Monthly Notices of the ROYAL ASTRONOMICAL SOCIETY

MNRAS **452,** 3726–3741 (2015) doi:10.1093/mnras/stv1084

A blind H I mass function from the Arecibo Ultra-Deep Survey (AUDS)

L. Hoppmann,[1,2★] L. Staveley-Smith,[1,3★] W. Freudling,[2★] M. A. Zwaan,[2] R. F. Minchin[4] and M. R. Calabretta[5]

[1]*International Centre for Radio Astronomy Research (ICRAR), M468, University of Western Australia, 35 Stirling Highway, Crawley, WA 6009, Australia*
[2]*European Southern Observatory (ESO), Karl-Schwarzschild-Str. 2, D-85748 Garching, Germany*
[3]*ARC Centre of Excellence for All-sky Astrophysics (CAASTRO)*
[4]*Arecibo Observatory, HC03 Box 53995, Arecibo, PR 00612, USA*
[5]*CSIRO Astronomy and Space Science, PO Box 76, Epping, NSW 1710, Australia*

Accepted 2015 May 11. Received 2015 May 4; in original form 2014 June 2

ABSTRACT

The Arecibo Ultra-Deep Survey (AUDS) combines the unique sensitivity of the telescope with the wide field of the Arecibo *L*-band Feed Array (ALFA) to directly detect 21 cm H I emission from galaxies at distances beyond the local Universe bounded by the lower frequency limit of ALFA ($z = 0.16$). AUDS has collected 700 h of integration time in two fields with a combined area of 1.35 deg^2. In this paper, we present data from 60 per cent of the total survey, corresponding to a sensitivity level of 80 μJy. We discuss the data reduction, the search for galaxies, parametrization, optical identification and completeness. We detect 102 galaxies in the mass range of $\log(M_{\rm H\,I}/M) - 2\log h = 5.6-10.3$. We compute the H I mass function (HIMF) at the highest redshifts so far measured. A fit of a Schechter function results in $\alpha = -1.37 \pm 0.03$, $\Phi^* = (7.72 \pm 1.4) \times 10^{-3}\,h^3\,{\rm Mpc}^{-3}$ and $\log(M^*_{\rm H\,I}/{\rm M}_\odot) = (9.75 \pm 0.041) + 2\log h$. Using the measured HIMF, we find a cosmic H I density of $\Omega_{\rm H\,I} = (2.33 \pm 0.07) \times 10^{-4}\,h^{-1}$ for the sample ($z = 0.065$). We discuss further uncertainties arising from cosmic variance. Because of its depth, AUDS is the first survey that can determine parameters for the HIMF in independent redshift bins from a single homogeneous data set. The results indicate little evolution of the comoving mass function and $\Omega_{\rm H\,I}$ within this redshift range. We calculate a weighted average for $\Omega_{\rm H\,I}$ in the range $0 < z < 0.2$, combining the results from AUDS as well as results from other 21 cm surveys and stacking, finding a best combined estimate of $\Omega_{\rm H\,I} = (2.63 \pm 0.10) \times 10^{-4}\,h^{-1}$.

Key words: galaxies: evolution – galaxies: ISM – galaxies: luminosity function, mass function – radio lines: galaxies.

1 INTRODUCTION

Understanding how and at what rate stars form from cool atomic and molecular gas ($<10^4$ K) is one of the crucial questions of modern astrophysics. The star formation rate (SFR) is well measured from UV, optical, infrared and radio continuum observations, and is found to increase by an order of magnitude over the redshift interval of $0 < z < 2.5$ (Hopkins & Beacom 2006). By comparison, the evolution of the atomic and molecular cosmic gas density appears to be less dramatic with recent galaxy evolution models suggesting that there may only be a weak evolution of cosmic gas density at $z < 2$ if there exists a self-regulated equilibrium between the inflow of gas into galaxies and the SFR (Obreschkow & Rawlings 2009; Power, Baugh & Lacey 2010; Lagos et al. 2011). However, better observations are necessary to further develop these models and to better understand the balance between gas accretion, star formation and feedback.

Measurements of the H_2 density (e.g. Keres, Yun & Young 2003) are unfortunately not easy, as the molecule does not possess a low-energy rotational transition. Instead, we are dependent on the use of CO as a proxy, with its uncertain dependence on optical depth, metallicity and the radiation field. More accurate observations are available for atomic hydrogen via damped Lyman α (DLA) systems at high redshift or via the 21 cm line in the local Universe.

DLAs are wide absorption features caused by high column densities of H I ($>2 \times 10^{20}$ atoms cm^{-2}) normally associated with galaxies. DLAs can be observed against bright background sources such as QSOs and appear to represent objects which contain the majority of H I at redshifts $1.6 < z < 5.0$. (Wolfe, Gawiser & Prochaska 2005) and are therefore an important reservoir for star formation.

★E-mail: laura.hoppmann@icrar.org (LH); Lister.Staveley-Smith@icrar.org (LS-S); wfreudli@eso.org (WF)

Table 1. Selection of major blind 21 cm spectral line surveys.

Survey	Reference	Telescope	N	Area (deg^2)	Redshift
AHISS[a]	Zwaan et al. (1997)	Arecibo	66	65	0–0.025
ADBS[a]	Rosenberg & Schneider (2002)	Arecibo	265	430	0–0.027
HIPASS[a]	Meyer et al. (2004)	Parkes	4315	21 341	0–0.042
North. HIPASS[a]	Wong et al. (2006)	WSRT	1002	7997	0–0.042
40 per cent ALFALFA[a]	Haynes et al. (2011)	Arecibo	10 119	2799	0–0.06
ALFALFA[b]	Giovanelli et al. (2005)	Arecibo	∼25 000	7000	0–0.06
AGES[b] WAPP	Auld et al. (2006)	Arecibo	∼1300	105	0–0.06
Mock			∼1300	95	0–0.16
CHILES[b] prec.	Fernández et al. (2013)	VLA	33	0.3	0–0.193
ALFA ZOA[b] shallow	Henning et al. (2010)	Arecibo	∼500	1000	0–0.06
deep			∼1500	280	0–0.16
AUDS[a] prec.	Freudling et al. (2011)	Arecibo	18	0.069	0.07–0.16

Notes. [a]Observations completed and survey completely published.
[b]Observations ongoing or data not completely published – survey results not finalized.

DLA measurements at $z \approx 4$ find values of $\Omega_{\rm H\,I}$ around double the local value (Zwaan et al. 2005). Prochaska, Herbert-Fort & Wolfe (2005) and Prochaska & Wolfe (2009) find a 50 per cent decrease to occur at lower redshifts $2.3 < z < 5.5$. However, Noterdaeme et al. (2012) use a larger Sloan Digital Sky Survey (SDSS) Data Release (DR) 9 sample and only find a 20 per cent decrease over a similar range. Measurements using Mg II systems at low-redshift DLA proxies are consistent with the latter (Rao, Turnshek & Nestor 2006), though selection effects are uncertain and errors are high. Nevertheless evolution in $\Omega_{\rm H\,I}$ above redshift $z > 0.5$ appears significantly lower than the corresponding evolution in the SFR.

Interpretation of 21 cm observations is more robust, but sensitivity considerations mean that observations are mainly limited to the local Universe. Examples of 21 cm surveys are summarized in Table 1. Extensive mapping of the sky has been done since the installation of multi-beam receivers on the Arecibo, Parkes and Effelsberg telescopes, which transformed these telescopes into powerful survey facilities. This resulted in a significant increase in the area surveyed and the number of galaxies detected. In terms of redshift, however, these surveys are still limited to $z \approx 0$. The two largest H I surveys are the H I Parkes All-Sky Survey (HIPASS; $z < 0.04$; Meyer et al. 2004; Wong et al. 2006) and the Arecibo Legacy Fast ALFA (ALFALFA; $z < 0.06$; Giovanelli et al. 2005). HIPASS detected 5317 galaxies in the southern and the northern sky up to a declination of $\delta = +25.5$. ALFALFA observed an area of ∼7000 deg^2 with the target of detecting about 30 000 galaxies at 21 cm.

Direct detections of galaxies beyond the local Universe are not only limited by sensitivity, but also by radio frequency interference (RFI) and receiver bandwidth. Target galaxies for deep 21 cm observations are therefore normally preselected. For example, Catinella et al. (2008) targeted galaxies up to $z = 0.25$ to look for the most H I-massive objects, selecting them by their Hα emission. Zwaan, van Dokkum & Verheijen (2001) and Verheijen et al. (2007) targeted clusters with redshifts about $z \approx 0.2$ to increase the chance of detection. Such a strategy leads to samples that are biased towards galaxies with high surface brightness in optical bands. Furthermore, in order to extend beyond the local Universe, such surveys need to be very sensitive. With that in mind, we commenced the Arecibo Ultra-Deep Survey (AUDS) – a blind 21 cm survey with the Arecibo *L*-band Feed Array (ALFA) to search for 21 cm H I line emission at redshifts between 0 and 0.16, the limit of the receiver. The AUDS precursor observations (Freudling et al. 2011) were an important test of the feasibility of such a survey. The precursor survey detected 18 galaxies in the redshift range $0.07 < z < 0.16$ with a total integration time of 53 h. While this provided a measurement of $\Omega_{\rm H\,I}$ in good agreement with measurements in the local Universe, the AUDS precursor was limited to a very small region with few detections and covered only a limited range of redshifts. Small number statistics and cosmic variance were therefore problems, resulting in large error bars.

In this paper, we present results of 60 per cent of the data from the full survey. It is a fully sampled and a significantly more sensitive data set than the precursor observation, providing a larger sample of direct 21 cm detections. The total integration time is eight times larger than that of the precursor survey. This paper allows a preliminary release for galaxies so far detected, and makes significant advances in the understanding of the evolution of the H I mass function (HIMF).

Throughout this paper, we use $H_0 = 100\,h\,{\rm km\,s^{-1}\,Mpc^{-1}}$, $\Omega_{\rm M} = 0.3$ and $\Omega_\Lambda = 0.7$.

1.1 Survey strategy

The primary goal of AUDS is to systematically survey the cosmic H I density ($\Omega_{\rm H\,I}$) in a volume that is beyond the local Universe to a sensitivity that has not been probed before. The strategy of the survey is therefore orthogonal to other current single-dish H I surveys in the sense that AUDS covers a very small area on the sky using the most sensitive 21 cm system currently available and using a very long integration time. Our goal was to achieve an exposure time of about 40 h per pointing, and a total of 1000 h of observing time (including overheads) was assigned to this project. To cover the field in the most uniform and sensitive way, we used the 'drift and chase' mode which we extensively tested and refined during our precursor observations (Freudling et al. 2011). The basic strategy was to carry out repeated drift scans over the same field. To optimize uniformity of the sky coverage, the feed array was rotated to ensure equal spacing between the beams. Due to the elliptical projection of the array on to the sky, the rotation angle varies between 15° and 23°. The orientation of the array relative to the scan direction is shown in Fig. 1.

One major difference with the precursor observations was that, with significantly more observing time available, we were able to Nyquist-sample the sky using short adjacent drift scans that were offset in declination by 0.1 of the beam size. This enabled much more accurate determination of source positions (limited only by signal-to-noise ratio, SNR) and source fluxes.

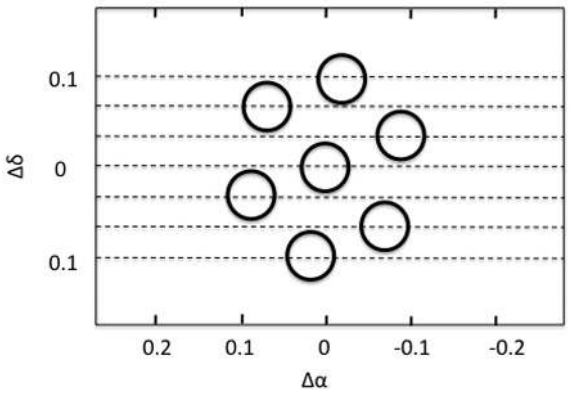

Figure 1. Idealized relative positions of the seven independent ALFA beams. For AUDS, the beams are rotated between 15° and 23° to achieve a uniform coverage of the survey area.

All observations were carried out at night time to achieve the best baselines and lowest system temperature. In order to be able to schedule observations for the project throughout the year, we elected to divide the total area into two fields at opposite right ascension within the SDSS footprint. The size of the individual field areas was determined by science goals and telescope limitations. A small area is required to go deep. On the other hand, the upper redshift limit of ALFA means that once sufficient sensitivity to low-mass galaxies is obtained, it is then better to go wide. Edge effects such as loss of sensitivity make it inefficient to consider fields which are smaller than half a square degree in size. Telescope start-up delays make it inefficient to consider drift scans much shorter than a degree in length.

1.2 Target selection and observations

The goal of AUDS is to carry out an unbiased, sensitive survey outside the local Universe. Our original goal was to be able to detect galaxies with $\sim 0.1 M^*_{M_{\rm H\,I}}$ of neutral hydrogen at the frequency limit of the ALFA receiver ($f = 1225$ MHz). In order to sample-independent volumes, we chose to observe two independent fields that contain no known clusters. Because of the long necessary integration times, the surveyed fields are necessarily small ~67 arcmin × 44 arcmin each, corresponding to a total volume of $V \approx 10^{3.9}$ Mpc^3. For efficient surveying, the two regions should differ in right ascension as much as possible, and be located at a declination where they can be tracked for the maximum time possible at Arecibo. Another criterion for the selection of our fields was that they were within the SDSS survey region. We also tried to avoid bright continuum sources as much as possible. The brightest continuum source is 43.9 mJy in Field 1 and 196.9 mJy in Field 2.

We used a 'drift and chase' mode for the observations. Each AUDS scan consists of 230 individual spectra for each beam and polarization, with each successive spectrum integrated over 1 s while the telescope covers 1 s in right ascension. The spectra from the seven ALFA beams were recorded using the Mock Spectrometer dividing each spectra into two intermediate-frequency (IF) sub-bands, each 172 MHz wide. The high-frequency IF is centred at $f = 1450$ MHz and the low-frequency IF is centred at $f = 1300$ MHz. Combined they cover the whole bandpass range of the ALFA receiver of 300 MHz with a spectral resolution of $\Delta f = 0.02$ MHz.

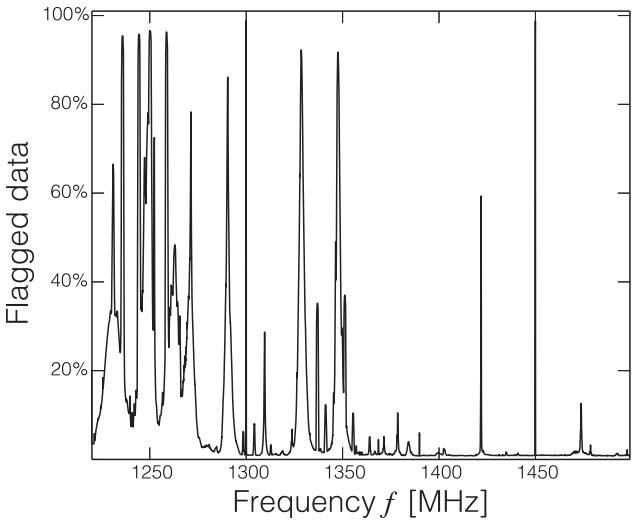

Figure 2. RFI occupancy plot for AUDS. While the higher frequency regions are only mildly affected by RFI, large regions of the lower frequency ranges are completely wiped out.

1.3 Data processing

The bandpass removal and calibration was done using the multibeam single-dish data reduction software LIVEDATA.[1] Details of the steps of the reduction process are described in Barnes et al. (2001). As LIVEDATA was originally developed to reduce data from the Parkes telescope for HIPASS, the program was adapted to suit the different settings of the Arecibo telescope including the handling of different types of FITS files and other Arecibo-specific issues such as calibration.

Each individual spectrum with 1 s integration time has a root mean square (rms) of about 50 mJy. To convert the individual spectra into regular gridded position–position–velocity cubes, we use the software GRIDZILLA[1]. For the final gridded data cubes, data from all beams and polarizations were combined.

GRIDZILLA calculates the contribution of every individual spectrum to each pixel of the grid and calculates the final value of the pixel based on the contributing spectra and the assigned weights. The weights were determined by the distance of spectra from the beam centre. We used a weighted median statistic to combine the spectra. The data values were first sorted, and their weights were summed. The weighted median is then the data value for which the sum of the weights is half the total weights. Barnes et al. (2001) have shown that using a median estimator was very successful for HIPASS in removing small amounts (less than 40 per cent) of bad data (caused by RFI, etc.) with the downside of increasing the noise level by at least 25.3 per cent.

However, on occasion, the AUDS data show much more significant levels of bad data (Fig. 2), especially in the frequency range of $f = 1220$–1350 MHz, necessitating further measures. Several sources of strong RFI, like the radar in Punta Salinas and transmissions from the nearby airport, interfere in this frequency range. Additionally, several satellites (e.g. *GPS*, *Galileo* and *GLONASS*) transmit in this frequency range. While the RFI emitted from the radar are narrow in frequency and pulsed in time, the RFI from the satellites span a wide frequency range, but do not occur at all times.

[1] http://www.atnf.csiro.au/computing/software/livedata

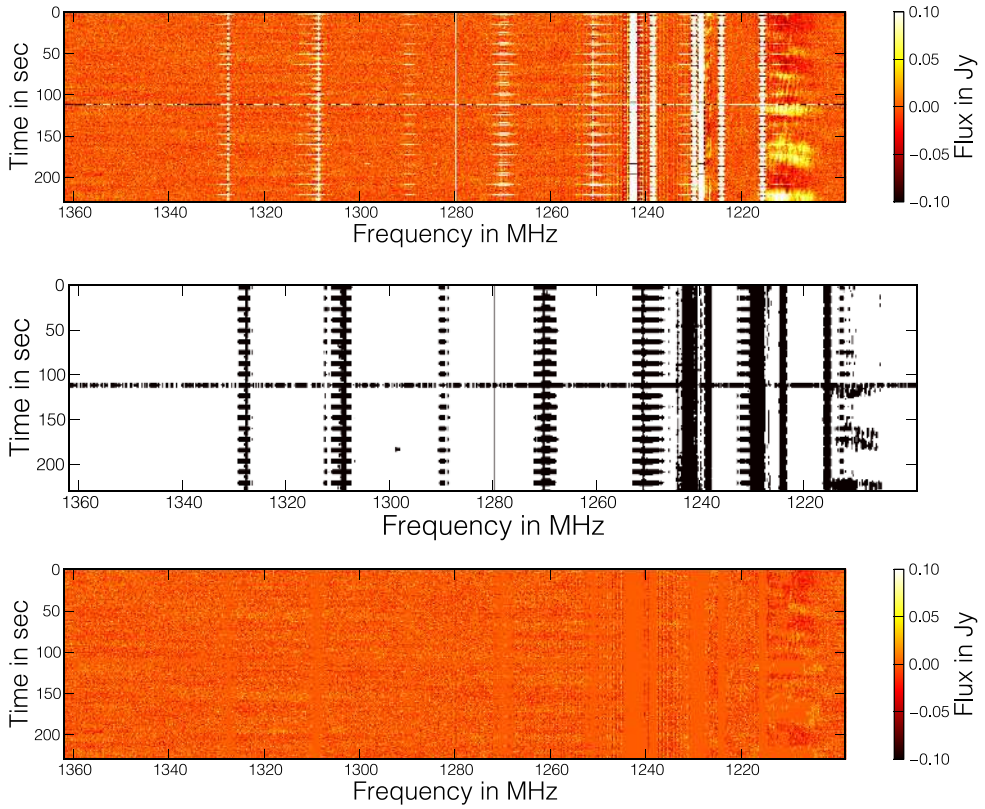

Figure 3. The three images show an example of the RFI flagging process. Upper panel: example of data from one beam after bandpass removal and calibration using LIVEDATA. A stack of 230 spectra is shown with 1 s integration time each. Centre panel: the 3σ mask created in the flagging process. The black regions will be masked out. Lower panel: data after masking with significantly reduced RFI.

To further mitigate against the RFI problem, we used a flagging routine applied to the bandpass-corrected data as follows.

(i) The rms in an RFI-free region is estimated. The RFI-free region was chosen by examination of several time–frequency images.
(ii) A 3.5σ mask is created where zero corresponds to valid pixels and one to masked pixels.
(iii) The mask is grown by smoothing it with a Hanning kernel of the size 5×5 pixel (time–frequency domain) which results in values between zero and one. Pixels where the values of the mask are above 0.1 are flagged and ignored during the gridding of the data.

This process is repeated three times before the data are gridded into data cubes. An example of the mask and flagging is shown in Fig. 3.

2 AUDS SAMPLE

2.1 Galaxy catalogue

To search for galaxies, position–velocity images were searched by eye to create a list of galaxy candidates. Due to the varying noise and strong RFI at higher redshift, available automated source finders were not able to create a usefully short candidate list. To create the source list, the cubes were searched by three members of the AUDS team. Each tried to identify every possible candidate, even those that were unlikely to be significant detections. Together, 294 unique candidates were identified and a preliminary source list was created. In a second step, a single person inspected each spectrum and image in position–velocity space from the merged list. Spectra were extracted and fitted and a shorter source list created based on the final inspection of each candidate. It was important to carefully distinguish between real galaxies and spurious detections based on their SNR, their spectral line shape and the shape of the detections in the image plane. Special attention was taken to distinguish between real sources and RFI. In many cases, a clear distinction was possible given their very different signatures in the position–velocity plane, RFI often being narrow in frequency and visible over large ranges in right ascension/declination. However, at low SNR, the distinction is not as clear. Candidates close to, or overlapping with, known RFI were treated especially carefully to ensure that they were real and that the bandpass was fitted correctly. This resulted in a shorter list of 133 likely candidates, 5 of which were common between the overlapping bands leaving 128 candidates.

We then used the completeness coefficient C, derived from the simulation discussed in Section 2.3, to create a final source list. C uses the integrated flux $S_{\rm int}$, the velocity width W and the rms σ of each galaxy to calculate the probability of detecting a galaxy in the survey. If $C > 0$, the galaxy was retained in the sample.

The final sample consists of 102 galaxies. A selection of spectra of AUDS galaxies is presented in Fig. 4. Parametrization of the galaxies was performed using the task `mbspect` which is part of the radio astronomy data reduction package MIRIAD (Sault, Teuben & Wright 1995).[2] The galaxy position estimated from the manual search was more precisely determined by fitting a Gaussian to the velocity integrated image (zeroth moment) over a width of 5–9 arcmin around

[2] http://www.atnf.csiro.au/computing/software/miriad/

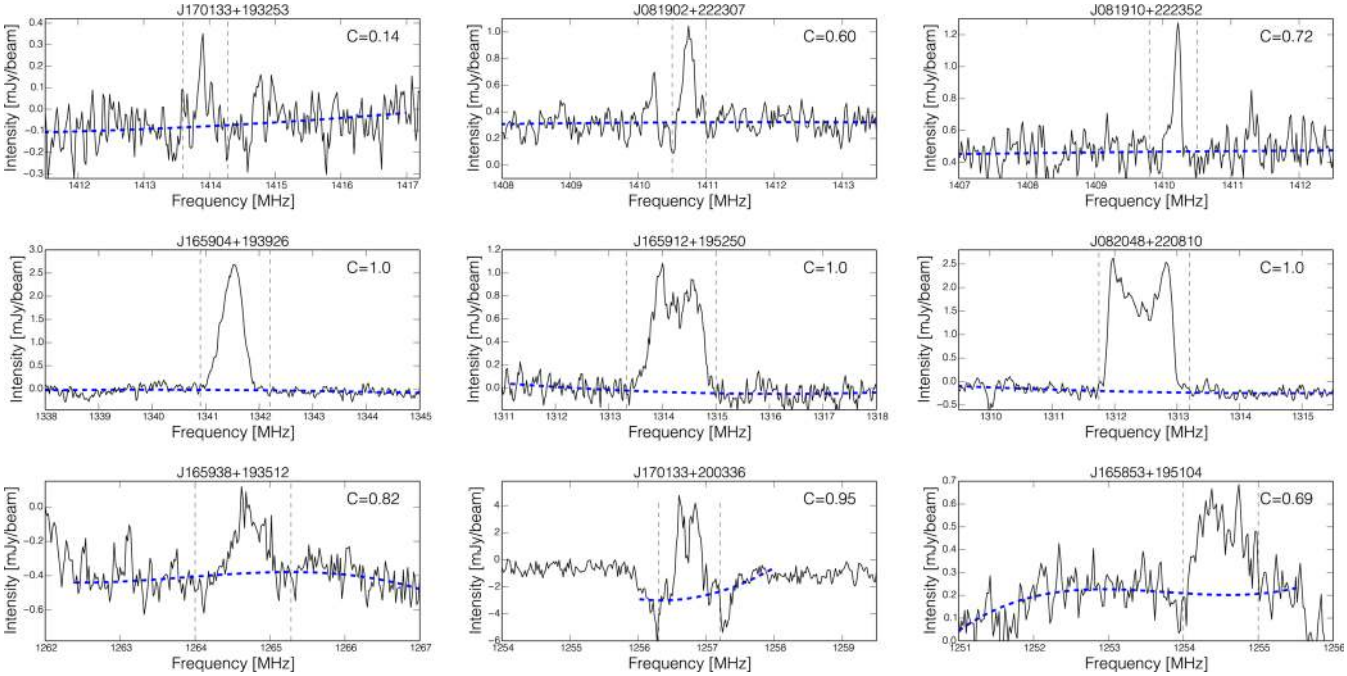

Figure 4. Selection of AUDS spectra. The black dashed vertical lines indicate the spectral range in which the line is fitted. This spectral region is excluded for the fit of the baseline, marked with the blue dashed line. The completeness coefficient for each galaxy is given in the upper-right corner. The top panels show the three lowest mass galaxies detected in the survey. The central panels show three galaxies at intermediate redshift with high SNR. The bottom panels show the three highest redshift galaxies.

the input position assuming that the galaxies are point sources. This is a good approximation as the beam size at the mean redshift of the galaxies in the sample ($z = 0.065$) is about $190\,h^{-1}$ kpc in diameter. Additionally, we also looked at the optical diameter (Petrosian diameter in the r band) of the AUDS galaxies we could cross-match to SDSS galaxies (details are given in Section 2.2) and found that 95 per cent of galaxies are smaller than 1.2 arcmin. This would allow the H I disc to exceed the optical diameter by up to three times and still be within the ALFA beam.

Next the spectra were optimally extracted, also using the MIRIAD function `mbspect`, at the new position using a window of 5–9 arcmin, weighting neighbouring pixels by the beam shape. The velocity range occupied by the detected galaxy was masked out, before a polynomial was fitted to the baseline. The spectral width W and the central velocity of the profiles were measured. The fit also provided $S_{\rm int}$, $S_{\rm peak}$ and the peak SNR. The fluxes were measured assuming that the galaxies are point sources. Using $S_{\rm int}$ and the luminosity distance $D_{\rm L}$ of the galaxies, we calculate $M_{\rm H\,I}$ as

$$\frac{M_{\rm H\,I}}{\rm M_\odot} = 49.8 \left(\frac{D_{\rm L}}{\rm Mpc}\right)^2 \left(\frac{S_{\rm int}}{\rm Jy\,Hz}\right). \quad (1)$$

The H I masses of the AUDS galaxies as a function of their distance are presented in Fig. 5.

The bivariant distributions as well as single-parameter histograms of the galaxy parameters (z, $S_{\rm int}$, $S_{\rm peak}$, W) are shown in Fig. 6. The redshift histogram shows that we did not detect any galaxies with $z > 0.13$. Detecting H I galaxies at high redshift proved challenging as the RFI environment at Arecibo is very hostile, especially for $f < 1290$ MHz.

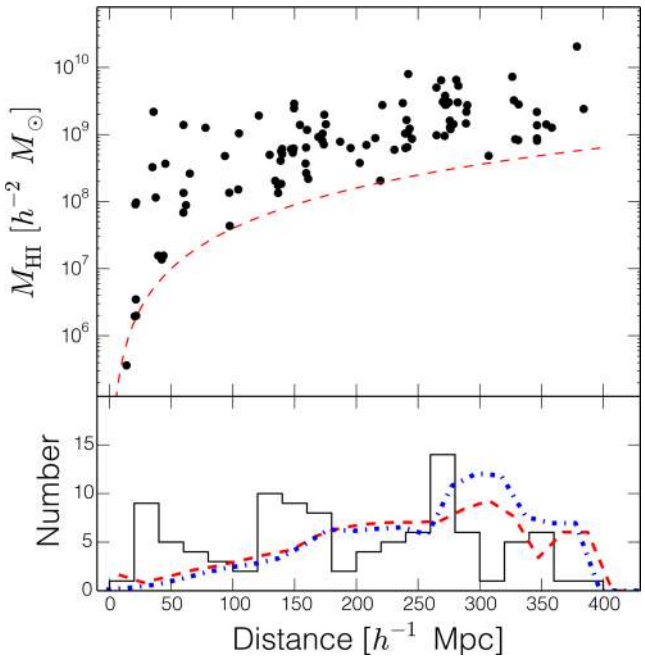

Figure 5. Top panel: H I masses of the AUDS galaxies as a function of distance. The red dashed line indicates the minimal detectable H I mass as a function of distance, assuming an integrated flux limit of $S_{\rm int} = 0.8$ mJy MHz. Bottom panel: the black solid histogram shows the distribution of detected galaxies. The red dashed line is the expected galaxy distribution derived by multiplying the 2DSWML selection function by $\Omega D^2 \Delta D \bar{n}$. The blue dash–dotted line is the prediction using the selection function from the $\sum 1/V_{\rm max}$ method.

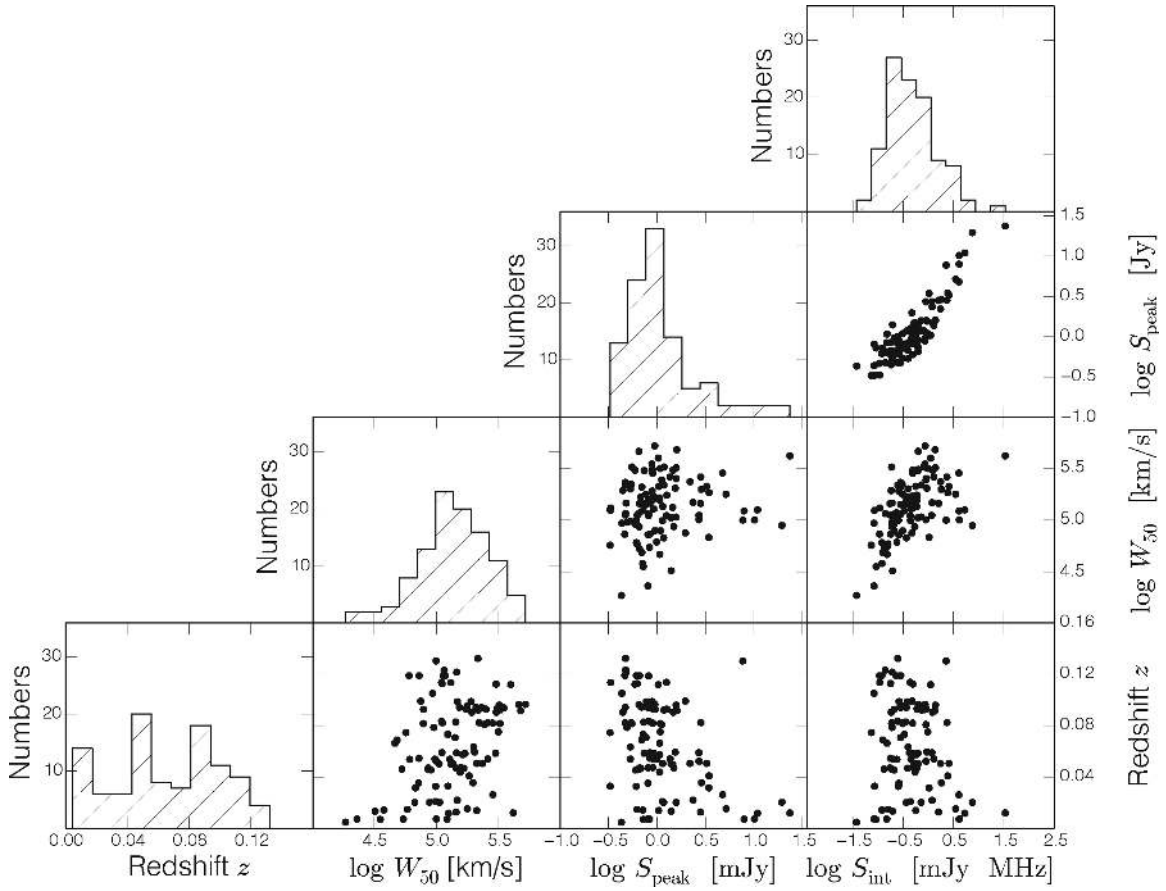

Figure 6. Log–log bivariate distribution of measured parameters of AUDS galaxies: redshift z, 50 per cent velocity width W_{50}, peak flux $S_{\rm peak}$ and integrated flux $S_{\rm int}$. On the diagonal the single-parameter histograms are plotted.

2.2 Optical counterparts

Both AUDS fields were chosen to overlap with the SDSS footprint. Searching the SDSS DR7 catalogue, we find that Field 1 has 25 galaxies and Field 2 has 56 galaxies with spectroscopic redshifts in the redshift range of AUDS. Additionally, there are 11 588 galaxies with only photometric redshifts in Field 1 and 9932 galaxies in Field 2.

We used the SDSS to find optical counterparts for the AUDS galaxies and found that 36 out of 102 have spectroscopically confirmed counterparts and that at least one of the AUDS galaxies is a pair. Optical galaxies are identified as matches when they are within a 2 arcmin radius around the H I position and the difference with the spectroscopic redshift is smaller than 150 km s^{-1}. Taking the position (inside the beam), the size, inclination and colour of the galaxy into account, we identify another 18 likely optical counterparts. Fig. 7 (left-hand panel) shows the offset between the position of the optical counterparts as given by the SDSS and the positions measured from the H I data for both the galaxies with optical counterparts with spectroscopic redshifts as well as the galaxies with likely counterparts with photometric redshifts. We also show the difference between the optical redshift and H I redshift in the right-hand panel of the same figure.

Even though the overall number of galaxies with reliable optical information is small, some trends are clearly visible (Fig. 8). There is a correlation between the detectability of a galaxy and its r-band luminosity as the SDSS is a magnitude but not volume-limited sample. This also becomes evident when one compares the luminosity of the optical counterparts with and without spectroscopic redshifts. Galaxies with higher masses at a certain redshift are more likely to have spectroscopic counterparts.

The second trend is that lower mass galaxies are predominately blue galaxies ($g - r < 0.7$) and less likely to have spectroscopic information. Redder galaxies are only found at large $M_{\rm H\,I}$. This is expected as bluer galaxies tend to be more gas rich. Red galaxies on the other hand tend to have lower gas mass fractions but are significantly more massive and luminous. That makes them easier to detect in optical surveys especially at higher redshift where the survey volume is larger. This means that non-volume-limited H I surveys tend to be biased against red galaxies with increasing redshift. We leave the more detailed discussion of optical properties as well as a stacking analysis for a later paper.

2.3 Survey completeness

The completeness of a survey is defined as the fraction of a certain type of galaxy which can be detected by a survey from the underlying distribution of objects down to the detection limit of the survey. Estimating the completeness of AUDS is a crucial step to understand the underlying galaxy population.

A good way to determine the completeness of the sample is to insert synthetic galaxies into the data and test the rate with which these galaxies are detected. This allows us to determine a completeness limit as a function of $S_{\rm int}$ as well as W and the single-pixel

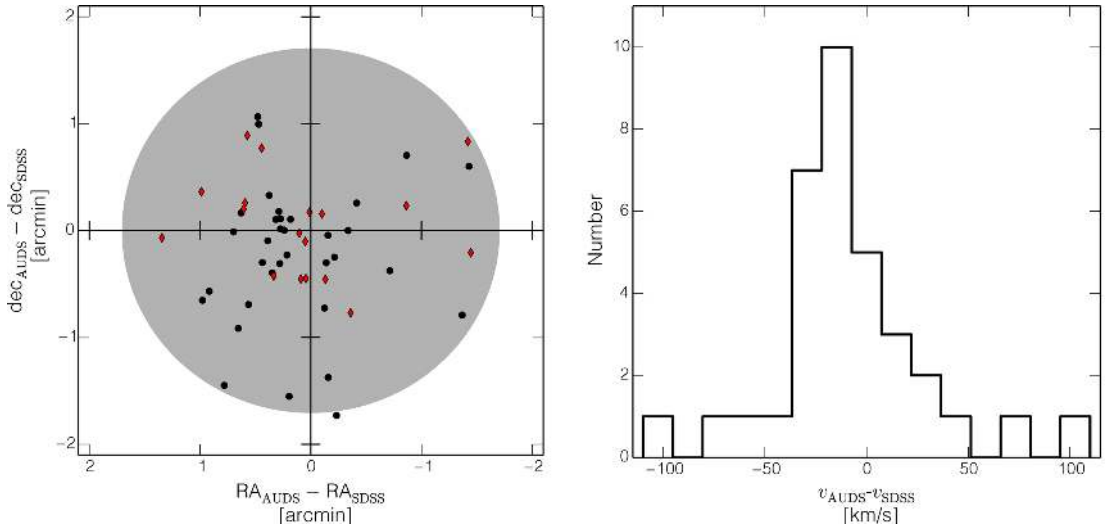

Figure 7. Left-hand panel: black dots: AUDS galaxies with spectroscopic counterparts; red diamonds: likely optical counterparts with only photometric redshifts. The plot shows the difference between the source position fitted to the AUDS galaxies and the source position given in the SDSS catalogue. The grey shaded region is the size of the ALFA beam. Right-hand panel: histogram of the difference in redshift between the measured optical velocity from SDSS and the AUDS for all galaxies with spectroscopic counterparts.

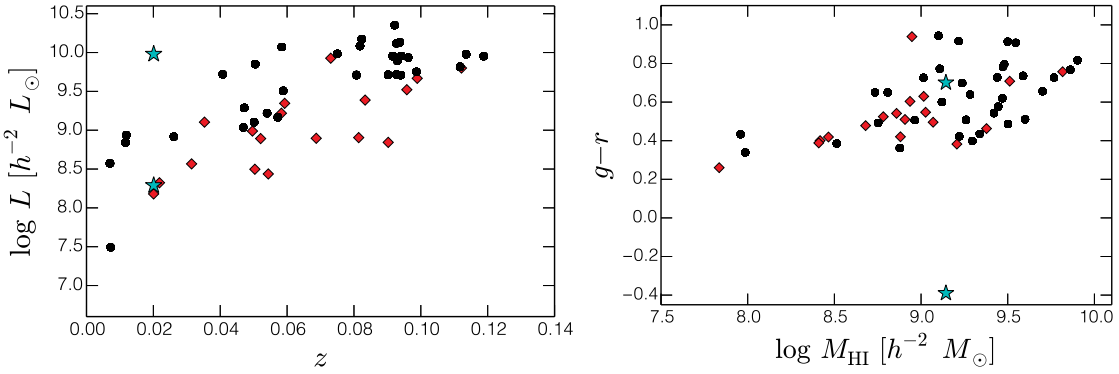

Figure 8. Optical counterparts of AUDS galaxies. Black dots: H I selected AUDS galaxies with optical spectroscopic counterparts; red diamonds: likely candidates with only photometric redshift measurements; cyan stars: galaxies in a pair. Left plot: AUDS is not volume limited and therefore we find a correlation between the redshift and the detected luminosity of the galaxy. Less luminous galaxies (at a certain redshift) are less likely to have spectroscopic counterparts. Right plot: lower mass galaxies are predominantly blue galaxies ($g - r < 0.7$). Redder galaxies are only found at larger $M_{\rm H\,I}$. As bluer galaxies tend to be more gas rich, they are more easily picked up at low masses in comparison to red galaxies which have lower gas mass fractions but are significantly more massive and luminous and therefore easier to detect at higher redshifts by optical surveys.

noise σ. To take the noise into account, we defined a noise-weighted integrated flux $S^*_{\rm int} = S_{\rm int}/\sigma$.

To insert the galaxies, we chose three representative subregions in the data cube of Field 1: one RFI-free region (1381 MHz), one region moderately affected by RFI (1325 MHz) and one region with high RFI occupancy (1231 MHz). Each region is 20 MHz wide. In total, 356 synthetic galaxies were inserted into the subcubes. The parameters for the synthetic galaxies were randomly chosen from an integrated flux range of $S_{\rm int} = 0$–1.5 mJy MHz and a width range of $W = 0.12$–2.0 MHz. Varying the width of the galaxies takes both variation due to different rotational velocities and that due to different inclinations into account. The shapes of the galaxy spectra were described by a busy function (Westmeier et al. 2014).

The data cubes were searched blindly in the same way as the original data cubes and 256 of the galaxies in the mock sample could be recovered. From the ratio of the number of detected galaxies ($n_{\rm d}$) to the number of all galaxies ($n_{\rm t}$), the completeness in logarithmic flux and linear W bins can be computed.

The dependence of the completeness on W and $S_{\rm int}$ as well as W and $S^*_{\rm int}$, shown in Fig. 9, resembles an error function shifted along the flux axis. We chose to describe the completeness function with the following analytic model:

$$C = \max(\mathrm{erf}(\alpha W^{\alpha}(S_{\rm int} - \beta W - \gamma)), 0) \quad (2)$$

$$C = \max(\mathrm{erf}(\alpha W^{\alpha}(S^*_{\rm int} - \beta W - \gamma)), 0). \quad (3)$$

The four independent parameters in equations (2) and (3) were chosen to fit the features in the binned completeness data namely: (1) the completeness decreases for smaller fluxes for all values of W, (2) W influences the steepness of the decrease of the completeness to zero (narrow profiles are easier to detect) and (3) the flux value at which the completeness essentially becomes zero.

The error bars in Fig. 9 indicate the 1σ binomial confidence interval given by $n_{\rm d}/n_{\rm t} \pm \sqrt{(p(1-p)/n_{\rm t})} = p$, with $n_{\rm d}$ being the number of detected synthetic galaxies in a bin, $n_{\rm t}$ the number of all synthetic galaxies in that bin and p the upper/lower limit of the

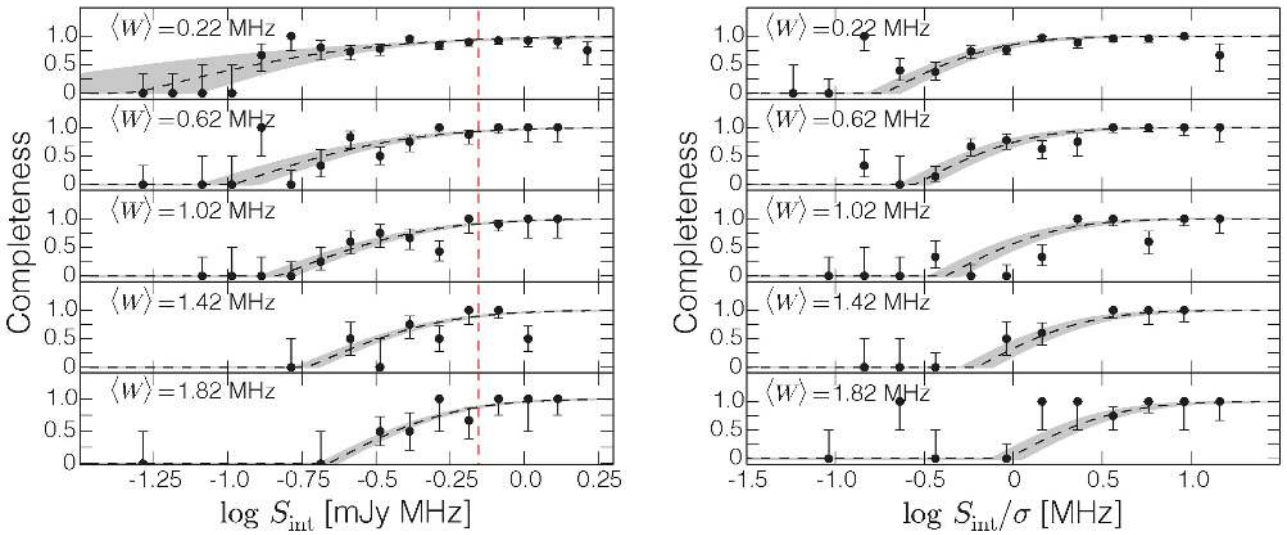

Figure 9. 1D slices of the completeness function in different bins of frequency width. The central width of each bin is given in the upper-left corner. The completeness is well described by an error function shifted along the horizontal axis. The grey shaded area indicates the completeness for the maximum and minimum width in the bin. Left-hand panel: the completeness as a function of $S_{\rm int}$ and W. The dashed line is the best fit to the data using equation (2). The red dashed line indicates a nominal completeness limit of $S_{\rm int} = 0.8$ mJy MHz. Right-hand panel: the completeness as a function of $S^*_{\rm int}$ and W. The dashed line is the best fit to the data using equation (3).

Table 2. Summary of the integrated fluxes at which a galaxy with a certain width reaches a completeness limit of 95, 90 and 65 per cent.

Width (MHz)	Width ($z = 0$) (km s^{-1})	$S_{\rm int}$ (mJy MHz)		
		$C = 0.95$	$C = 0.90$	$C = 0.65$
0.22	46	0.76	0.49	0.18
0.62	131	0.81	0.58	0.28
1.02	215	0.87	0.65	0.35
1.42	300	0.93	0.71	0.40
1.82	384	0.98	0.77	0.45

confidence interval. Binning data in intervals of $\Delta S_{\rm int} = 0.1$ mJy MHz and $\Delta W = 0.4$ MHz and fitting equation (2) gives the best-fitting parameter of $\alpha = 28.95$, $\beta = -0.08$, $\gamma = -5.21$ and $\delta = 0.29$. Using the noise-weighted flux ($\Delta S^*_{\rm int} = 0.2$, $\Delta W = 0.4$ MHz) and fitting equation (3) gives the best-fitting parameter of $\alpha = 68.39$, $\beta = 0.45$, $\gamma = -0.52$ and $\delta = 0.030$. Since the noise changes throughout the cube, we found that equation (3) is the better way to minimize the effect of the different noise levels and we therefore used $C(S^*_{\rm int}, W)$ when calculating the HIMF. For each galaxy in the sample, we calculate the completeness coefficient by inserting the value for $S_{\rm int}$, σ and W into equation (3) giving us a specific value for that galaxy which represents the probability of detecting this galaxy in the sample. Additionally, we give the integrated flux at which a galaxy of a certain width reaches a completeness of $C = 95$, 90 and 65 per cent in Table 2. As before, only galaxies with completeness coefficients >0 have been accepted in the sample (see Section 2.1). Some of the galaxies with a completeness coefficient = 0 may in fact be real, but it is not possible to use them for statistical studies.

2.4 Reliability

One method of estimating the reliability of an H I survey is to use optical information provided by other large surveys, e.g. SDSS. Another possibility is to re-observe parts of the survey area to assess the reliability of their sources and the measured parameters, done for example by HIPASS (Zwaan et al. 2004). However, neither of these methods are feasible for AUDS. The spectral density of SDSS in the area of the AUDS fields is too low to systematically cross-match all the optical and H I selected galaxies (Section 2.2), and using additional telescope time for re-observations is not practical.

As a first step to estimate the reliability, we therefore looked at the overlap regions between the low- and the high-frequency bands. The cubes overlap in the frequency range of 1368–1382 MHz. In this overlapping region, we find five galaxies which are individually detected in both the high- and the low-frequency bands. There are two additional galaxies in the source list which are only detected in the high-frequency bands. However, both these galaxies have a completeness coefficient $C < 0.3$.

Next we estimated the reliability of our survey re-using the list of possible detections created from the data cubes with inserted synthetic objects (see Section 2.3). Of the total of 330 detected sources, 256 turned out to be synthetic and 12 were previously detected AUDS galaxies. Of the 62 unidentified source candidates, about 10 passed the criteria for being included in our first cut candidate list as described in Section 2.1. None of them passed our criteria to be included in the final catalogue, otherwise they would be considered as one of the detected AUDS galaxies. We find that the number of such false detections is roughly proportional to the number of confirmed detections in any of the volumes. Therefore, we conclude that first cut catalogues contain of the order of $10/256 \backsimeq 4$ per cent false detections, and the number of false detections in the final catalogue will be lower than that. We therefore consider 96 per cent as a lower limit for the reliability of AUDS. The impact of false detections in AUDS is negligible for all results presented in subsequent sections.

2.5 Cosmic variance

Measurements of the galaxy density in a finite volume are affected by the large-scale structure of the Universe causing a bias in

measurements in small volumes like AUDS. The sample variance originating from a finite volume is called cosmic variance. In order to quantify the cosmic variance of the density measurement, a quantity ξ can be defined as $\xi\,[\mathrm{per\ cent}] = 100 \times \sigma_{\mathrm{var}} / \langle N \rangle$ with the variance $\sigma^2_{\mathrm{var}} = \Sigma_i(\langle N \rangle - N_i)^2/n$, with $\langle N \rangle$ being the mean galaxy count in the selected volumes, N_i the number of galaxies in the volume i and n the total number of selected volumes.

To estimate ξ in our sample, we selected 100 random fields in the SDSS North Galactic Pole field (using DR7) with the same size and redshift range as one of the AUDS fields. We then calculated the mean and standard deviation of the number of galaxies in these fields. To estimate the sampling error in ξ and σ_{var}, we repeated that procedure 1000 times. The number of galaxies per random field varied between 10 and 335 galaxies with an average number of $54(\pm2) \pm 23(\pm3)$ galaxies or a sample variance of $\xi = 42 \pm 5$ per cent. Doing the same test, selecting two AUDS-sized fields as in the survey reduces the cosmic variance to $\xi = 29 \pm 4$ per cent. The decrease in cosmic variance corresponds to a reduction of $\sqrt{2}$. Comparing these results to the information from our fields, we find that our fields are slightly denser than the average field of the same size in SDSS. We find 58 galaxies in Field 1 (1.1 times overdense) and 60 galaxies (1.2 times overdense) in Field 2.

We compare our results to those presented by Driver & Robotham (2010). They derived an empirical expression for ξ for galaxy surveys using the spectroscopic redshifts of galaxies from the DR7 SDSS in the redshift range of $0.03 < z < 0.1$. They found that ξ is mainly influenced by the survey volume, the survey aspect ratio and whether the survey area is contiguous or consists of several independent volumes. Using their equation, we find $\xi = 33$ per cent for both fields, or $\xi = 46$ per cent which is within 1σ of our result.

The sample variation in the AUDS fields suggests that any density result will be correspondingly biased. However, a correction is possible as follows.

(1) We selected a large subsample from the spectroscopic DR7 SDSS galaxy sample ($L1$). $L1$ is in the main SDSS field ($130^\circ < \alpha < 236^\circ$, $0^\circ < \delta < 58^\circ$) selected to maximize the area (5150 deg^2) but to avoid the complex shape of the edges of SDSS (see Driver & Robotham 2010). Even though SDSS is not completely immune to cosmic variance itself, $L1$ is large enough that the expected difference between the mean density of $L1$ and that of the Universe is $\sim$7 per cent based on the results of Driver & Robotham (2010).

(2) We selected all SDSS galaxies in small fields surrounding each of the AUDS fields. We name these smaller SDSS fields $S1$ and $S2$. The area of $S1$ and $S2$ needs to be larger than the area of the original AUDS fields to reduce Poisson noise due to the small number of galaxy counts, but small enough such that their density remains correlated with the density of galaxies in the AUDS fields. To find the optimum size of $S1$ and $S2$, we placed 100 AUDS-like volumes at random positions within SDSS. We then computed the average galaxy density of each AUDS-like volume. Around each of these 100 AUDS-like fields, we placed another field of a larger size. For each field, we calculated the ratio of the density of the AUDS-sized field to the larger field surrounding it. Repeating this procedure for differently sized field 250 times, we found that the standard deviation of the density ratio is minimized (at 11 per cent) when the size of the surrounding field is 4.2 deg^2. That is, the quadrature sum of Poisson noise and cosmic variance is lowest for this field size. Furthermore, the density ratio itself indicates that $S1$ and $S2$ are representative of the structure in the smaller field.

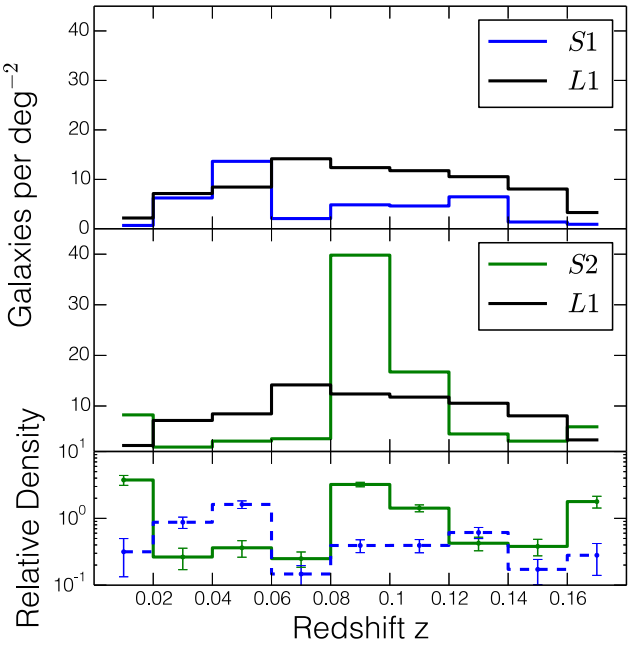

Figure 10. Comparison between the normalized numbers of galaxies in the $\sim$4.2 deg^2 sized SDSS fields $S1$ and $S2$ (surrounding two AUDS fields) and the representative SDSS field with a total area of 5150 deg^2 ($L1$). Top panel: comparison between Field 1 (blue line) and SDSS (black line); centre panel: comparison between Field 2 (green line) and SDSS (black line). Bottom panel: the relative density ratio for fields $S1$ and $S2$ compared to the representative field $L1$.

Table 3. To correct our HIMF for the effect of cosmic variance, we calculated the relative density in redshift bins for both AUDS fields individually. We compared the number of galaxies per deg^2 in redshift bins in the small fields ($S1$, $S2$) around the AUDS fields and a large field ($L1$) to detect over- or underdense regions in $S1$ and $S2$. We derive the density ratio ρ_S/ρ_L of the AUDS field (Field 1, Field 2) in relation to a representative SDSS galaxy sample and its dependence on the redshift.

z	ρ_{S1}/ρ_{L1}	ρ_{S2}/ρ_{L1}
0.0–0.02	0.316	3.754
0.02–0.04	1.004	0.264
0.04–0.06	1.835	0.363
0.06–0.08	0.147	0.249
0.08–0.10	0.430	3.216
0.10–0.12	0.453	1.422
0.12–0.14	0.439	0.424
0.14–0.16	0.230	0.380
0.16–0.18	0.350	1.783

(3) We compared the number of galaxies per area in redshift bins in the small fields ($S1$, $S2$) and the large field ($L1$) to detect over- or underdense regions in $S1$ and $S2$ (Fig. 10, Table 3). It is important to note that we make the assumption that the optically selected fields ($S1$, $S2$ and $L1$) have the same distribution of galaxies as the H I selected AUDS sample. Looking at the respective redshift bins for each field, we find the relative density of the small fields to vary between being 4.3 times underdense and 3.8 times overdense in comparison to the representative SDSS field ($L1$). Tracing the relative density in the AUDS fields in redshift bins allows us to correct for the effect in the HIMF as described in Section 3.1.

For this correction, we make the assumption that optical data and the H I data correlate. To test this assumption, we compare the bias factor for the SDSS fields ($S1, S2, L1$) with derived bias parameters for H I selected surveys. Seljak et al. (2005) measured the bias parameter for optical galaxies as a function of luminosity. Using their bias factors, we find that the average bias factor of the galaxies in the 4.2 deg^2 regions around the AUDS fields is $\langle b_{S1,\,S2}\rangle = 0.97 \pm 0.11$ while the $L1$ field has an average bias of $\langle b_{L1}\rangle = 0.99 \pm 0.06$. Observations as well as numerical simulations estimate local bias parameters of the neutral hydrogen relative to the dark matter between 0.7 and 1.0, with a typical uncertainty of ± 0.2 (Basilakos et al. 2007; Martin et al. 2012; Davé et al. 2013, see also Padmanabhan, Choudhury & Refregier 2015, for review). This shows that the clustering between optical selected galaxies and dark matter, and that between H I selected galaxies and dark matter are very similar on the spatial scales probed here, and therefore allow us to use the optical data to correct for over-/underdensities in the H I selected galaxies.

3 H I MASS FUNCTION (HIMF)

3.1 Methods

The HIMF $\Phi(M_{\rm H\,I})$ is a measure of the number of galaxies per unit volume dV for a given $M_{\rm H\,I}$ and is a crucial input parameter for models and simulations describing galaxy formation and evolution. We derived the HIMF in comoving coordinates to avoid changes in the measured densities purely caused by the expansion of the Universe.

The HIMF is often parametrized by a Schechter function defined as

$$\Phi(M_{\rm H\,I}) = \ln 10\, \Phi^* \left(\frac{M_{\rm H\,I}}{M_*}\right)^{\alpha+1} {\rm e}^{-\frac{M_{\rm H\,I}}{M_*}}, \quad (4)$$

with the faint-end slope α, the characteristic mass $M^*_{\rm H\,I}$ and the normalization Φ^*.

We use two different methods to derive the HIMF: the $\sum 1/V_{\rm max}$ method (Schmidt 1968) and the 2D stepwise maximum likelihood (2DSWML; Zwaan et al. 2003).

The basic $1/V_{\rm max}$ method assigns each galaxy a weighting factor which corresponds to the inverse maximum volume ($V_{\rm max}$) in which a galaxy can be detected inside the survey volume.

We adapt this method to compute the maximum search volume using the relation for completeness in equation (3). The completeness for a galaxy changes if the galaxy is shifted to a different part of the cube as the noise changes within the field and with frequency.

We therefore create two additional data cubes of the same size as the original cubes. In the first one, each pixel value corresponds to the comoving volume in Mpc^3 corresponding to that pixel. In the second data cube, each pixel value corresponds to the rms noise of neighbouring pixels. The noise is computed by calculating the rms noise in a ± 250 km s^{-1} range around that pixel. For each galaxy, we computed the expected completeness C_i if that galaxy were placed at any of the pixels within the survey volume using equation (3). For that purpose, we scaled $S_{\rm int}$ and W to the distance corresponding to each pixel, and used the rms of that pixel in the noise cube. The effective volume per pixel is then the product of completeness and volume V_i for each galaxy.

The volume in which a given galaxy is detectable, hereafter called the 'detectable volume', is then the sum over the effective volume of each pixel,

$$V_{\rm max} = \sum_i C_i \times V_i. \quad (5)$$

The comoving HIMF is then defined as the sum over the $M_{\rm H\,I}$ range of all galaxies j in an $M_{\rm H\,I}$ bin with the bin size $\Delta M_{\rm H\,I}$,

$$\Phi(M_{\rm H\,I}) = \sum_j \frac{1}{V_{{\rm max},\,j}}. \quad (6)$$

In addition to the volume cube, we also created a cosmic-variance-corrected volume cube. For the cosmic-variance-corrected cube, we multiplied each volume pixel in a redshift bin with the relative density of that redshift bin found in the optical sample (Table 3),

$$V_{\rm max,CV}[z_1, z_2] = \frac{\rho_S[z_1, z_2]}{\rho_L[z_1, z]} V_{\rm max}[z_1, z_2]. \quad (7)$$

This means that the volume of a pixel in an underdense region is 'shrunk' while the volume of a pixel in an overdense regions is 'enlarged'. The $\sum 1/V_{\rm max}$ method has the advantage of being fast and simple to implement as well as producing a normalized HIMF.

The second method to calculate the HIMF is the SWML method developed by Efstathiou, Ellis & Peterson (1988) as a superior tool to derive the luminosity functions of galaxies. The idea behind the SWML technique is to find the function $\Phi(M_{\rm H\,I})$ that yields maximal joint probability of detecting all galaxies in the sample. It has the advantage over the $1/V_{\rm max}$ method because the results are independent variables of density. In the SWML method, the galaxy mass distribution is split into bins assuming a constant distribution in each bin. It is not necessary to assume a functional form for the HIMF. Based on SWML method, Zwaan et al. (2003) developed the 2DSWML method which solves for the space density of $M_{\rm H\,I}$ and W at the same time.

3.2 $\sum 1/V_{\rm max}$ HIMF

Fig. 11 shows the results of the HIMF calculation using the $\sum 1/V_{\rm max}$ method. In the following, we will exclude the lowest mass data point in our fit as it only contains one galaxy with a low completeness coefficient (see Fig. 4, upper-left panel). Nevertheless, this galaxy and the two in the next bin are suggestive of a possible upturn in the HIMF.

The error bars were calculated using Poisson statistics not taking into account measurement errors (e.g. distance and $M_{\rm H\,I}$). The best Schechter fit to the model without correction for cosmic variance is $\alpha = -1.53 \pm 0.04$, $\log(M^*_{\rm H\,I}/{\rm M}_\odot) = (3.52 \pm 0.80) + 2\log h$ and $\Phi^* = (3.52 \pm 0.80) \times 10^{-3}\, h^{-3}\,{\rm Mpc}^{-3}$. The errors in the Schechter function are computed using a jackknife technique, de-selecting one galaxy at a time (Quenouille 1949).

Next we use the cosmic-variance-corrected volumes ($V_{\rm max,\,CV}$) to compute the HIMF (Fig. 11). Both measurements show good agreement within the error bars. The result for the best fit to the cosmic-variance-corrected data is $\alpha = -1.37 \pm 0.03$, $\log(M^*_{\rm H\,I}/{\rm M}_\odot) = (9.75 \pm 0.041) + 2\log h$ and $\Phi^* = (7.72 \pm 1.4) \times 10^{-3}\, h^3\,{\rm Mpc}^{-3}$.

We binned the data in 0.5 dex bins of $M_{\rm H\,I}$ starting at an H I mass of 5.5. Different binning and starting masses give slightly different mass functions and fits. We estimated the error caused by this by varying the starting mass in the range of $\log(M_{\rm H\,I}/{\rm M}_\odot) = (5-5.5) + 2\log h$ and the bin size by 2–5 bins per dex in $M_{\rm H\,I}$. The

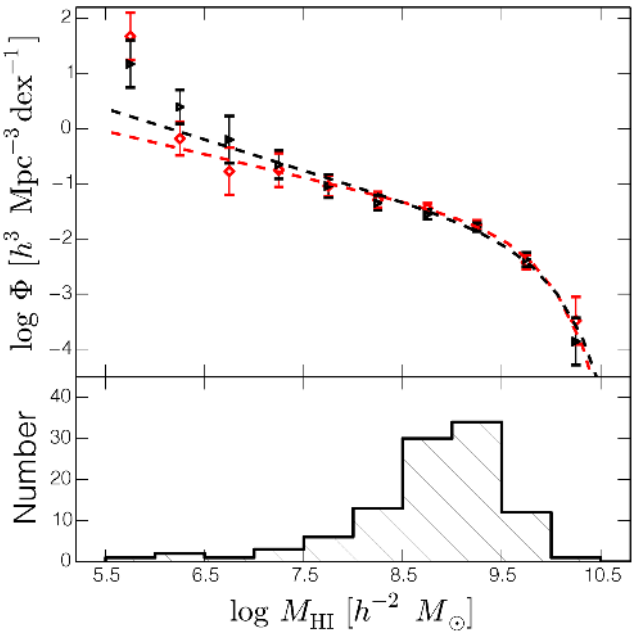

Figure 11. Top panel: the AUDS comoving HIMF measured using the $\Sigma\, 1/V_{\rm max}$ method (black triangles) and $\Sigma 1/V_{\rm max,\,CV}$ method (red diamonds), with their corresponding best-fitting Schechter functions. The error bars indicate the 1σ uncertainties based on Poisson statistics. The black dashed line is the best-fitting Schechter function for the $\Sigma\, 1/V_{\rm max}$ with $\alpha = -1.53 \pm 0.04$, $\Phi^* = (3.52 \pm 0.80) \times 10^{-3}\, h^3\,{\rm Mpc}^{-3}$ and $\log(M^*_{\rm H\,I}/{\rm M}_\odot) = (9.87 \pm 0.02) + 2\log h$. The red dash–dotted line is the best-fitting Schechter function for the $\Sigma\, 1/V_{\rm max,\,CV}$ method with $\alpha = -1.37 \pm 0.03$, $\Phi^* = (7.72 \pm 1.4) \times 10^{-3}\, h^3\,{\rm Mpc}^{-3}$ and $\log(M^*_{\rm H\,I}/{\rm M}_\odot) = (9.75 \pm 0.041) + 2\log h$. Bottom panel: histogram of H I masses, using the same binning as in the top panel.

rms over the best fits was comparable to the fitting error ($\sigma_\alpha = 0.04$, $\sigma_{\log M^*_{\rm H\,I}} = 0.10$ and $\sigma_\Phi = 4.6 \times 10^{-3}\, h^3\,{\rm Mpc}^{-3}$).

3.3 2DSWML HIMF

The 2DSWML method is independent of density variations due to large-scale structure and therefore a good, independent test to check the results from the $\Sigma\, 1/V_{\rm max}$ method. It does, however, rely on the shape of the HIMF not changing. Furthermore, the difference in the noise at different locations within the survey volume cannot be taken into account. Instead, we used a single value for the rms for each detected galaxy.

We recovered the normalization for the HIMF using the mean galaxy density $\bar{n}$. $\bar{n}$ is calculated by correcting the measured distribution of galaxies with the selection function $S(D)$ (Section 3.3.1). Davis & Huchra (1982) presented several estimators to calculate $\bar{n}$. We choose the $\overline{n_3} = N_{\rm total}/\int S(D)\,{\rm d}V$ estimator as it is the most stable one for small numbers even though it has a slight dependence on large-scale structure.

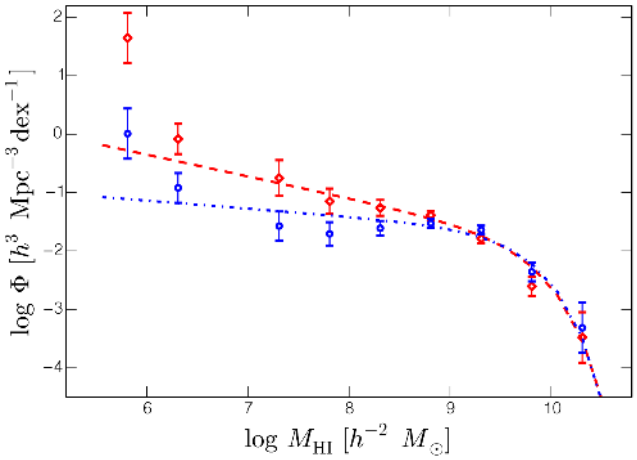

Figure 12. Comparison between the H I mass functions derived with the $\Sigma 1/V_{\rm max,\,CV}$ method (red diamonds and dashed line) and with the 2DSWL method (blue dots and dash–dotted line, respectively). The lines indicate the best-fitting Schechter functions.

Fig. 12 compares the 2DSWML HIMF and the $\Sigma\, 1/V_{\rm max,\,CV}$ HIMF. We find that the data points for both methods are in reasonably good agreement at the high-mass end ($M_{\rm H\,I} > 10^{9.5}\,{\rm M}_\odot$) with each other (Table 4). At lower masses, the slope of the 2DSWML (red dashed line) is less steep. Even though most of the data points agree with each other within the 1σ error bar, the 2DSWML HIMF points are systematically lower causing a significant difference in the fitted slope. The best fit to the 2DSWML HIMF function yields $\Phi^* = (9.82 \pm 5.40) \times 10^{-3}\, h^3\,{\rm Mpc}^{-3}$, $\log(M^*_{\rm H\,I}/{\rm M}_\odot) = (9.70 \pm 0.07) + 2\log h$ and $\alpha = -1.14 \pm 0.10$. The good agreement between the normalization of the 2DSWML and the $\Sigma\, 1/V_{\rm max,\,CV}$ HIMF is encouraging, as the normalization for the 2DSWML HIMF was calculated independently.

3.3.1 *Selection function*

The selection function $S(D)$ is the probability that a galaxy at a distance D is detected by the survey. We calculate $S(D)$ for the 2DSWML and the $\sum 1/V_{\rm max}$ HIMF as described in Zwaan et al. (2003).

Assuming a homogeneous space distribution of galaxies, the number of galaxies observed in a distance bin of the size ΔD at the distance D is $n(D) = \Omega\, D \Delta D\, \bar{n}\, S(D)$ with the solid angle Ω and the average number of galaxies $\bar{n}$. Fig. 5 compares the detected and the predicted redshift distribution showing that they are not in good agreement.

The galaxy numbers derived by the selection function give lower numbers of nearby galaxies while overestimating galaxies at larger distances in comparison to the detected galaxy distribution. The effects could be caused by large-scale structure which are not traced by the selection function. A good example is the overdensity at $D \approx 270$ Mpc in the AUDS histogram which does not show up

Table 4. Comparison between the best Schechter fit and the values for $\Omega_{\rm H\,I}$ for the derived AUDS HIMF.

Methods	α	$\log(M^*_{\rm H\,I}/{\rm M}_\odot) + 2\log h$	Φ^* ($10^{-3}\, h^3\,{\rm Mpc}^{-3}$)	$\Omega_{\rm H\,I}$ (int.) ($10^{-4}\, h^{-1}$)	$\Omega_{\rm H\,I}$ (sum.) ($10^{-4}\, h^{-1}$)
$\Sigma\, 1/V_{\rm max}$	-1.53 ± 0.04	9.87 ± 0.02	3.52 ± 0.80	1.76 ± 0.09	1.63 ± 0.08
$\Sigma\, 1/V_{\rm max,\,CV}$	-1.37 ± 0.03	9.75 ± 0.041	7.72 ± 1.4	2.22 ± 0.10	2.33 ± 0.07
2DSWML	-1.14 ± 0.10	9.70 ± 0.07	9.82 ± 5.40	1.96 ± 0.51	1.94 ± 0.49

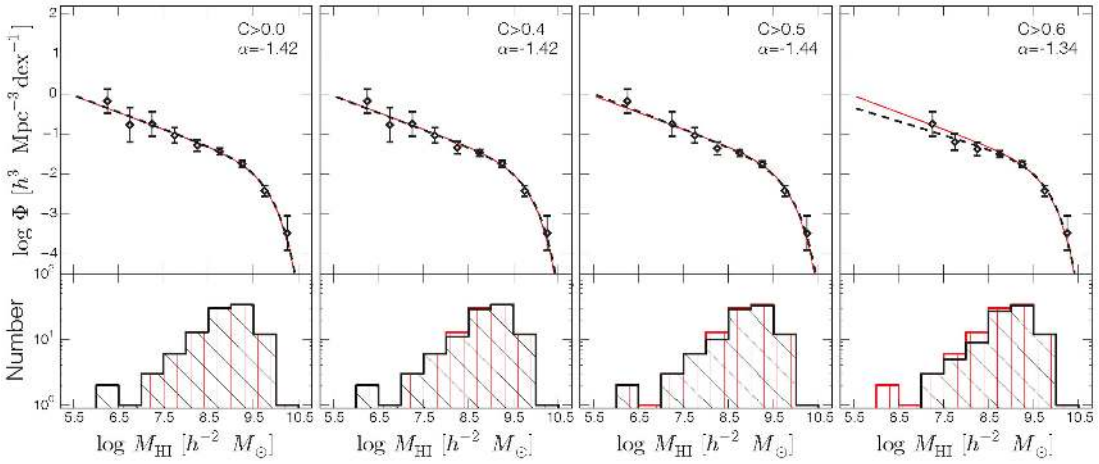

Figure 13. The $1/V_{\rm max,\,CV}$ HIMF calculated for galaxies selected with different completeness cutoffs. The completeness equation (3) was used to measure the completeness coefficient C for each galaxy. Plots for $C > 0, 0.4, 0.5$ and 0.6 are shown. The corresponding numbers of galaxies are 102, 98, 96 and 92. The Schechter fits are shown as the black dotted lines with the result of the fitted slope in the top-right corner of each panel. The red solid line is the Schechter fit from Fig. 11, based on all galaxies with $C > 0$. The red histograms show the H I mass distribution of the full AUDS sample and the black histograms are the corresponding distributions for the restricted samples.

in the prediction. A possible explanation for the overestimation of high-redshift galaxies lies in the general limitation of AUDS to pick up galaxies at high redshift largely caused by RFI, as described in Section 2.1.

3.4 Influence of completeness

We rate the quality of our detected galaxies by their completeness coefficient C and only include galaxies with $C > 0$, excluding the lowest mass galaxy for the HIMF fit. In Fig. 13, we compare the $1/V_{\rm max,\,CV}$ HIMF for different cuts in the completeness coefficient ($C = 0.4, 0.5, 0.6$). The plot shows that the lower mass galaxies ($M < 10^{9.5}\,{\rm M}_\odot$) are excluded first causing the slope to flatten. High completeness cutoffs ($C > 0.5$) exclude galaxies with masses around the knee of the HIMF resulting in smaller values for the normalization Φ^*. The change in the HIMF with completeness is an intriguing result as unlike HIPASS and ALFALFA; the low-mass AUDS galaxies are located well beyond the local volume and may represent more typical volumes in the Universe.

3.5 Evolution of the HIMF

The redshift range of AUDS allows us to split the sample into redshift bins to see evolutionary trends. We split our sample at the mean redshift of our sample ($z = 0.065$). This creates a lower redshift bin with 52 galaxies and a mean redshift of $z = 0.036$ and higher redshift bin with 50 galaxies and a mean redshift of $z = 0.095$. The binning by redshift indirectly means we divide the galaxies by their mass, as the faint galaxies can only be detected close by while rarer, massive galaxies need the large volume of the high-redshift bin to be found.

However, there is some overlap over a mass range of 10^8–$10^{10}\,{\rm M}_\odot$ as can be seen in Fig. 14. There appears to be evidence for only a modest change in the HIMF. Formally, if α and $M^*_{\rm H\,I}$ are held fixed at their best-fitting value for the whole sample, Φ^* is ∼16 per cent lower for the higher redshift sample. Any change in the density of galaxies with H I mass $>10^{10}$ or $<10^8\,{\rm M}_\odot$ cannot be explored. The full AUDS sample will provide tighter limits on the amount of evolution that can arise from feedback processes in galaxies over this redshift range (Kim et al. 2013).

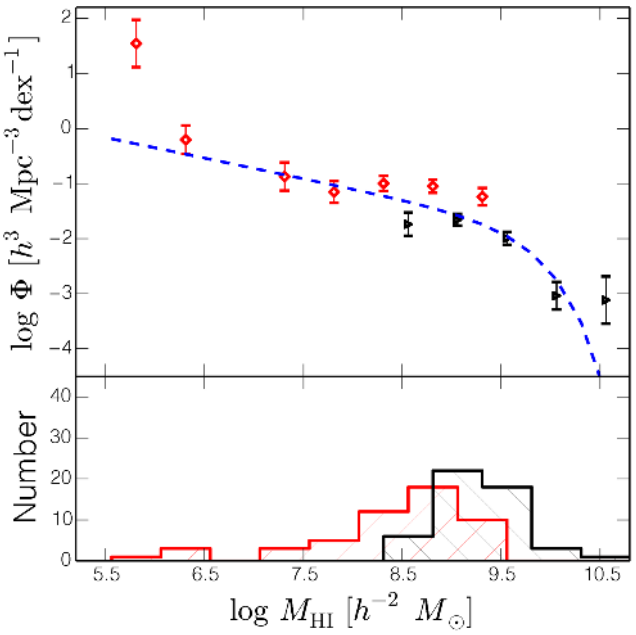

Figure 14. Top panel: comparison between the HIMF derived from the low-redshift (red diamonds) and high-redshift (black triangles) subsample. The blue dashed line is the fit to the complete AUDS sample (Fig. 11). In the mass range of 10^8–$10^{10}\,h^{-2}\,{\rm M}_\odot$, the low-redshift HIMF is significantly higher than the high-redshift HIMF. The discrepant high-redshift bin at $10^{6.75}\,h^{-2}\,{\rm M}_\odot$ only contains one galaxy. Bottom panel: the number distribution of the low-redshift sample ($\langle z\rangle = 0.036$) in red and the high-redshift sample ($\langle z\rangle = 0.094$) in black.

3.6 Comparison of HIMF

The HIMF is a useful tool to describe how much H I is locked up in galaxies. The slope of the HIMF gives the relative importance

Table 5. Comparison of different results for the HIMF from 21 cm surveys.

Survey	Reference	α	$\log(M^*_{\rm H\,I}/{\rm M}_\odot) + 2\log h$	Φ^* $(10^{-3}\,h^3\,{\rm Mpc}^{-3})$
AHISS	Zwaan et al. (1997)	-1.2	9.55	14
ADBS	Rosenberg & Schneider (2002)	-1.53	9.63	11.9
	Springob, Haynes & Giovanelli (2005)	-1.24	9.68	9.3
HIPASS	Zwaan et al. (2005)	-1.37 ± 0.03	9.55 ± 0.02	14.2 ± 1.9
ALFALFA	Martin et al. (2010)	-1.33 ± 0.02	9.71 ± 0.01	14.0 ± 0.9
AUDS	This work	-1.37 ± 0.03	9.75 ± 0.041	7.72 ± 1.4

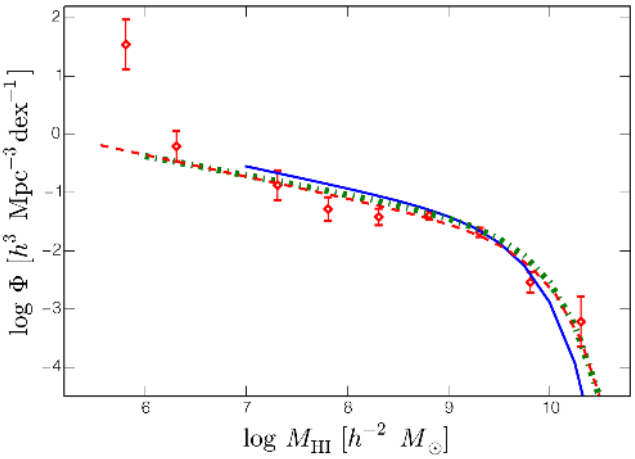

Figure 15. Comparison between the AUDS HIMF (red diamonds and red dashed line) and the best-fitting Schechter functions from HIPASS (blue solid line) and ALFALFA (green dot–dashed line). The individual data points of the HIMF agree (within the error bars) with the two surveys in the local Universe, apart from a small number of low H I mass AUDS galaxies.

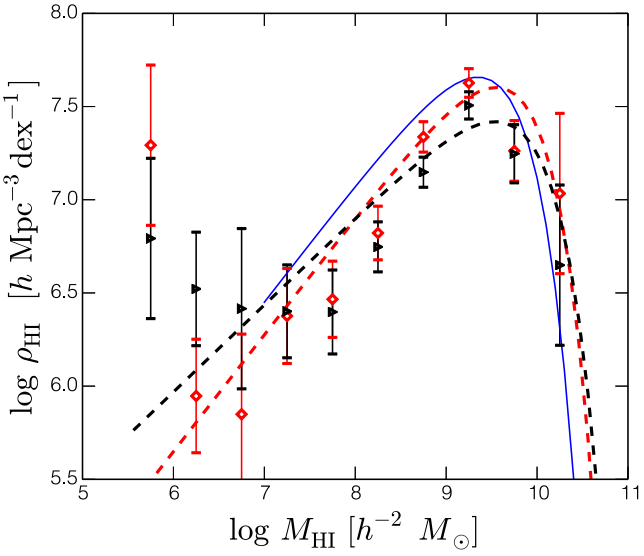

Figure 16. The distribution of the H I mass density as a function of $M_{\rm H\,I}$. The H I mass density is derived by multiplying the HIMF by the centre of each $M_{\rm H\,I}$ mass bin. The red diamonds and dashed line show the mass density derived from the $\Sigma 1/V_{\rm max,\,CV}$ method and the black diamonds and dashed line correspond to the $\sum 1/V_{\rm max}$ method. The blue line indicates the H I mass density from HIPASS. The comparison shows that for AUDS there is a slightly higher contribution from both faint and bright galaxies to the overall H I density.

of low-mass and high-mass galaxies. Table 5 presents an overview over the measured HIMF from different surveys. An early HIMF measured from the AHISS survey (Zwaan et al. 1997) found a flat faint-end slope of $\alpha = -1.2$. The Arecibo Dual-Beam Survey (ADBS; Rosenberg & Schneider 2002) found a much steeper slope of $\alpha = -1.53$. However, both these surveys suffer from small numbers and small volumes.

The two largest blind H I surveys HIPASS and ALFALFA (40 per cent) find slopes $\alpha = -1.37 \pm 0.03$ (Zwaan et al. 2005) and $\alpha = -1.33 \pm 0.02$ (Martin et al. 2010), respectively. The good agreement between the two surveys seems to suggest that the slope of the HIMF in the local Universe is well defined. However, at the high-mass end the ALFALFA survey reveals a larger number of galaxies than HIPASS (Fig. 15). Martin et al. (2010) explain this difference with the higher upper redshift limit and larger volume in comparison to HIPASS.

The AUDS sample allows us to construct an HIMF for the first time which is independent of the local volume and at much higher redshifts and to higher sensitivities than previous surveys. Fig. 15 compares the results from AUDS with the best fit of HIPASS and ALFALFA. AUDS measures a slightly steeper slope α than HIPASS or ALFALFA, but overall the surveys agree well with each other. We find a tentative rise at very low masses caused by faint, low-mass galaxies detected in our survey, which might have been missed in previous, less sensitive surveys. Twice as many galaxies are detected compared to the prediction from the extrapolated HIMF. Unfortunately, the overall small-number statistics make it necessary to interpret this result with caution. Although the detected faint galaxies are well beyond the Local Group, the volume sampled at this mass level is only about 8 h^{-3} Mpc^3, so the cosmic variance is high.

4 COSMIC H I DENSITY $\Omega_{\rm H\,I}$

4.1 H I mass density ($\rho_{\rm H\,I}$) and cosmic H I density ($\Omega_{\rm H\,I}$)

Fig. 16 shows the H I mass density $\rho_{\rm H\,I}$ for different H I masses; we compare the results before and after cosmic variance correction. The lines indicate the best fit to $\rho_{\rm H\,I}$ using equation (4). The measured slope of the HIMF has important implication for the contribution to the H I mass density $\rho_{\rm H\,I}$ of low-mass galaxies. The measured slope of the AUDS sample shows that the gas mass density is dominated by galaxies with masses around $10^{9.7}\,h^{-2}\,{\rm M}_\odot$ corresponding to the knee of the HIMF. Comparing the results of AUDS and HIPASS (Fig. 16) shows differences between the two surveys. AUDS detects more galaxies at the low-mass end and also detect slightly more galaxies at the very high mass end.

The total H I mass density can then be computed by integrating the best Schechter fit using $\rho_{\rm H\,I} = \Gamma(\alpha+2) \times \Phi^* M^*_{\rm H\,I}$, where Γ is the Euler Gamma function and α, Φ^* and $M^*_{\rm H\,I}$ the fit parameters from the Schechter fit. This gives $\rho_{\rm H\,I} = (6.24 \pm 0.23) \times 10^7\, h\, {\rm M}_\odot\, {\rm Mpc}^{-3}$ for the $\sum 1/V_{\rm max}$ method and $\rho_{\rm H\,I} = (6.53 \pm 0.31) \times 10^7\, h\, {\rm M}_\odot\, {\rm Mpc}^{-3}$ for $\sum 1/V_{\rm max,\,CV}$. We estimated the error using the jackknifing technique as with the HIMF calculation (Section 3.2).

In addition to this, we can also calculate $\rho_{\rm H\,I}$ by summing over individual data points in the H I density distribution. The results are $\rho_{\rm H\,I} = (4.46 \pm 0.21) \times 10^7$ and $(5.78 \pm 0.20) \times 10^7\, h\, {\rm M}_\odot\, {\rm Mpc}^{-3}$ for the uncorrected and corrected values, respectively. The results of the summation and integration of $\rho_{\rm H\,I}$ agree within the 1σ error bars indicating that our survey was able to adequately probe below the knee of the HIMF to capture most of $\Omega_{\rm H\,I}$.

To compare our results to other measurements, we compare the comoving H I density, $\rho_{\rm H\,I}$, to the current ($z = 0$) critical density of the Universe, $\rho_{\rm crit,\,0}$, to derive the cosmic H I density,

$$\Omega_{\rm H\,I} = \frac{\rho_{\rm H\,I}}{\rho_{\rm crit}(z=0)} = \frac{8\pi G}{3H_0}\rho_{\rm H\,I}, \quad (8)$$

where G is the gravitational constant and H_0 is the Hubble constant at $z = 0$. Note that the definition of $\Omega_{\rm H\,I}$, consistent with previous work, simply scales the comoving density by the current critical density and not by the comoving, redshift-dependent critical density. We find $\Omega_{\rm H\,I} = (1.63 \pm 0.08) \times 10^{-4}\, h^{-1}$ before correction and $\Omega_{\rm H\,I} = (2.33 \pm 0.07) \times 10^{-4}\, h^{-1}$ after cosmic variance correction, summing up the data points. As noted in Section 2.5 the cosmic variance correction has formal uncertainties of 8 per cent in piggybacking to the larger 4.2 deg^2 SDSS field (11 per cent for a single field, 8 per cent for two fields) and 7 per cent for SDSS as a whole (Driver & Robotham 2010), giving rise to a combined systematic uncertainty of 11 per cent. However, there are additional factors due to differing bias factors for H I and optical surveys, and unknown stochasticity factors which may raise this overall uncertainty (see Chang et al. 2010) which are neglected in this paper.

4.2 Evolution of the cosmic H I density $\Omega_{\rm H\,I}$

To trace the evolution of cool gas with cosmic time, we split our sample into different bins of redshift. For each subsample, we derived the HIMF and calculated $\Omega_{\rm H\,I}$. As the number of the galaxies in the redshift bins is relatively small, we decided to fit the HIMF with a Schechter function keeping $M^*_{\rm H\,I}$ and α fixed using the results we found for the $\sum 1/V_{\rm max,\,CV}$ and only fit the normalization Φ^*. $\Omega_{\rm H\,I}$ is then calculated by integrating over the Schechter function. First we split the sample into two redshift bins at the mean redshift of the sample ($\langle z \rangle = 0.065$), creating two samples with mean redshifts of $\langle z \rangle = 0.036$ and 0.095. We find $\Omega_{\rm H\,I} = (3.68 \pm 0.39) \times 10^{-4}\, h^{-1}$ for the low-redshift sample and $\Omega_{\rm H\,I} = (1.93 \pm 0.19) \times 10^{-4}\, h^{-1}$ for the high-redshift sample. The results indicate a possible decrease in $\Omega_{\rm H\,I}$ towards the upper end of the redshift range of the sample.

Next we selected the eight highest redshift galaxies between the redshifts of 0.119 and 0.132 to probe the high-redshift end of our sample. Integrating over the Schechter function, we find $\Omega_{\rm H\,I} = (2.24 \pm 0.78) \times 10^{-4}\, h^{-1}$. Due to the small numbers of galaxies in this bin, Poisson scatter is the dominant source of error. We also selected a low redshift with the eight lowest redshift galaxies. The result is $\Omega_{\rm H\,I} = (5.33 \pm 1.89) \times 10^{-4}\, h^{-1}$ agreeing well with results from HIPASS and ALFALFA as well as the AUDS lower redshift bin.

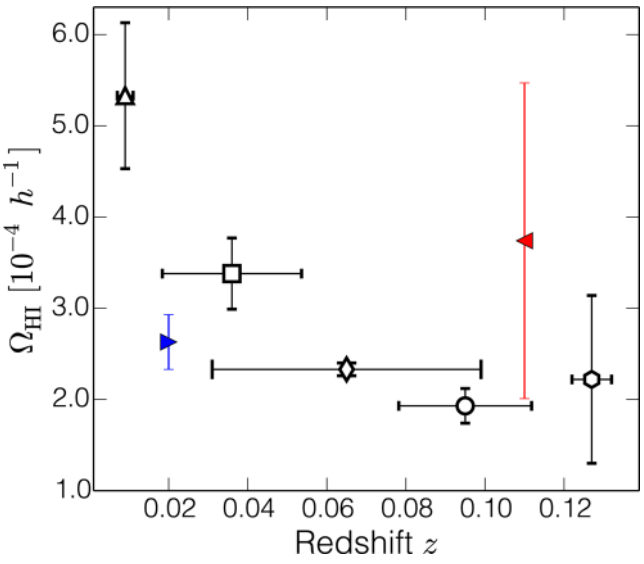

Figure 17. Measurements of $\Omega_{\rm H\,I}$ for different redshift bins in AUDS (black points). Note that not all data points are independent from each other but overlap in redshift (see Table 4). The mean redshifts of the subsamples are $z = 0.009$ (triangle), $z = 0.036$ (square), $z = 0.065$ (diamond), $z = 0.095$ (circle) and $z = 0.127$ (hexagon). Comparing the results to HIPASS (blue right-pointing triangle) and the AUDS precursor (red left-pointing triangle) shows little evolution in the measurements from $z = 0$ to 0.16.

Table 6. Results for $\Omega_{\rm H\,I}$ binning the sample in different redshift bins for AUDS.

Δz	$\langle z \rangle$	Number	$\log \frac{M_{\rm H\,I}}{{\rm M}_\odot} + 2\log h$	$\Omega_{\rm H\,I}$ ($10^{-4}\, h^{-1}$)
0–0.013	0.009	8	6.3–9.3	5.33 ± 1.89^a
0–0.065	0.036	52	6.3–9.5	3.68 ± 0.39^b
0.065–0.132	0.095	53	8.4–10.3	1.93 ± 0.19^b
0.119–0.132	0.127	8	8.9–10.3	2.24 ± 0.78^a
0–0.132	0.065	102	6.3–10.3	2.33 ± 0.07^b

Notes. [a]Errors derived using Poisson statistics.
[b]Errors derived using jackknifing.

The results for $\Omega_{\rm H\,I}$ for different redshift bins are summarized in Fig. 17 as well as Table 6. Note that the measurements of the eight high- and eight low-redshift galaxies are not independent of the data binned at the mean redshift of the sample. It appears likely from this comparison that the low-redshift points are high compared with those at higher redshift. The HIPASS result agrees better with the high-redshift points suggesting that there is no evolution detected and that the low-redshift results may be subject to cosmic variance errors.

4.3 Discussion

Measuring $\Omega_{\rm H\,I}$ and its evolution with redshift has long been an important scientific question. 21 cm measurements at low redshift provide a good constraint for $\Omega_{\rm H\,I}$ in the local Universe. Beyond that measurements have been more difficult. Until very recently there has been a huge gap between these local measurements and

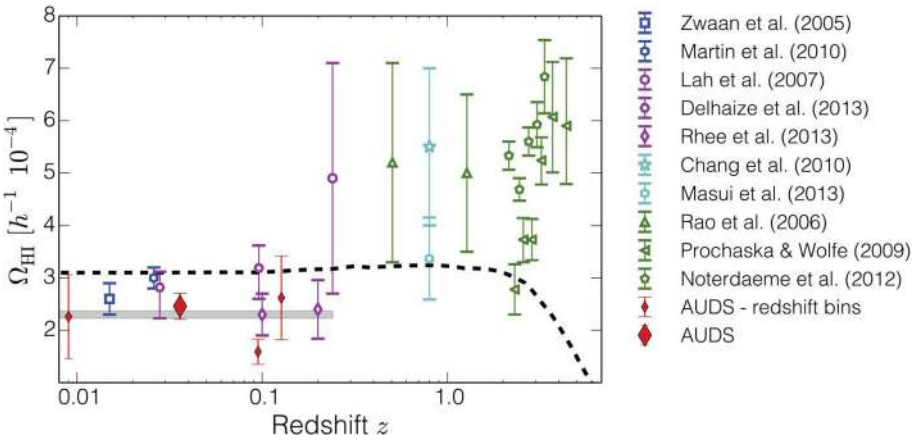

Figure 18. Evolution of the cosmic $\Omega_{\rm H\,I}$ density with redshift. The colour corresponds to the type of measurement. Blue: blind 21 cm surveys; magenta: H I stacking; cyan: intensity mapping; green: measurements from Lyα absorption spectra; red: AUDS. We present the result using the complete AUDS sample (single thick diamond) as well as the binned results (thin diamonds). Observations show no significant evolution in $\Omega_{\rm H\,I}$ out to $z = 0.2$. Calculating the best combined estimate based on all measurements of $\Omega_{\rm H\,I}$ out to this redshift, we find the 1σ interval marked in grey. The black dashed line is the prediction presented by Lagos et al. (2014), using semi-analytic models described in Lagos et al. (2012).

Table 7. Overview of measurements of $\Omega_{\rm H\,I}$ up to a redshift of $z = 0.2$. We calculate a weighted mean of the individual measurement to find a universal value of $\Omega_{\rm H\,I}$ for this redshift range.

Reference	$\langle z \rangle$	$\Omega_{\rm H\,I}$ ($10^{-4}\,h^{-1}$)	Method
Zwaan et al. (2005)	0.015	2.6 ± 0.3	Sources
Martin et al. (2010)	0.025	3.0 ± 0.2	Sources
Freudling et al. (2011)	0.111	3.74 ± 1.70	Sources
Delhaize et al. (2013)	0.028	$2.82^{+0.30}_{-0.59}$	Stacking
Delhaize et al. (2013)	0.096	$3.19^{+0.43}_{-0.59}$	Stacking
Rhee et al. (2013)	0.1	2.3 ± 0.4	Stacking
Rhee et al. (2013)	0.2	2.4 ± 0.6	Stacking
This paper	0.034	3.68 ± 0.39	Sources
This paper	0.095	1.93 ± 0.19	Sources
Best combined estimate	0–0.2	2.63 ± 0.10	

measurements at high redshift $z > 1.5$ using DLA measurements. Moreover, this period is marked by a significant change in SFR and therefore interesting for galaxy evolution studies. Successful attempts have been made using the stacking technique to bridge that intermediate redshift gap (Delhaize et al. 2013; Rhee et al. 2013) as well as the intensity mapping technique (Chang et al. 2010; Masui et al. 2013) at higher redshift (Fig. 18).

AUDS is the first survey which begins to probe this redshift range using direct detections (Fig. 18). The AUDS results combined with the low-redshift 21 cm surveys imply only limited, if any evolutionary effects out to $z = 0.2$, corresponding to a look-back time of $1.7\,h^{-1}$ Gyr.

We use these measurements (Table 7) to calculate a weighted average for $\Omega_{\rm H\,I}$ for $0 < z < 0.2$. Weighing each measurement by its error, we find $\Omega_{\rm H\,I} = (2.63 \pm 0.10) \times 10^{-4}\,h^{-1}$. The result is presented in Fig. 18 as the grey shaded region indicating the 1σ level. The black dashed line shows the results from semi-analytic models presented by Lagos et al. (2014), using their model as described in Lagos et al. (2012). They also find a very weak increase in $\Omega_{\rm H\,I}$ over this redshift range, in agreement with the observational result for $\Omega_{\rm H\,I}$.

5 CONCLUSIONS

In this paper, we present early results from AUDS, a deep blind 21 cm line survey of two selected fields in the redshift range between 0 and 0.16 with a sensitivity of 80 μJy. We detected a total of 102 galaxies with masses within $\log(M_{\rm H\,I}/{\rm M}_\odot) - 2\log h = 5.6{-}10.3$. We used synthetic galaxies to derive a completeness function based on $S_{\rm int}$, W and σ. We used the SDSS DR7 to correct the sample for cosmic variance and derived a $\sum 1/V_{\rm max,\,CV}$ HIMF which is well fitted by a Schechter function with the parameters $\alpha = -1.37 \pm 0.03$, $\Phi^* = (7.72 \pm 1.4)\,10^{-3}\,h^3\,{\rm Mpc}^{-3}$ and $\log(M^*_{\rm H\,I}/M) = (9.75 \pm 0.041) + 2\log h$, a result which is in good agreement with results from local surveys (HIPASS, ALFALFA).

The comoving H I mass density at the mean redshift of the sample is $\rho_{\rm H\,I} = (5.78 \pm 0.20) \times 10^7\,h\,{\rm M}_\odot\,{\rm Mpc}^{-3}$ contributing a fraction $\Omega_{\rm H\,I} = (2.33 \pm 0.07) \times 10^{-4}\,h^{-1}$ of the critical density of the Universe. The depth of the survey allows for the first time the derivation of both the shape and normalization of the HIMF from a blindly surveyed volume outside of the local Universe. In the volume that excludes the local Universe, at $z > 0.06$, AUDS probes the mass range within $\log(M_{\rm H\,I}/{\rm M}_\odot) - 2\log h = 8{-}10.3$. The derived HIMF is indistinguishable from that derived from local surveys. These observations constitute strong evidence that the HIMF did not rapidly evolve in the last billion years.

At redshifts up to 0.005, AUDS probes the HIMF at masses as low as $\log(M_{\rm H\,I}/{\rm M}_\odot) = 5.6 + 2\log h$. We detected twice as many galaxies as predicted from the local HIMF for $\log(M_{\rm H\,I}/{\rm M}_\odot) < 7 + 2\log h$. This might be an indication that the HIMF rises more steeply than previously thought at the very low mass end. If correct, this finding implies that the fraction of $M_{\rm H\,I}$ contributed by low-mass galaxies may be more significant than previously appreciated.

ACKNOWLEDGEMENTS

We want to thank Ensieh Vaez for help with source finding. LH wants to thank Jacinta Delhaize and Stefan Westerlund for coding assistance as well as the ASA for providing travel support. The Arecibo Observatory is operated by SRI International under a cooperative agreement with the National Science

Foundation (AST-1100968), and in alliance with Ana G. Méndez-Universidad Metropolitana, and the Universities Space Research Association. This research was partially supported by the ESO DGDF fund. This research made use of the Sloan Digital Sky Survey archive. The full acknowledgement can be found at http://www.sdss.org.

REFERENCES

Auld R. et al., 2006, MNRAS, 371, 1617
Barnes D. G. et al., 2001, MNRAS, 322, 486
Basilakos S., Plionis M., Kovač K., Voglis N., 2007, MNRAS, 378, 301
Catinella B., Haynes M. P., Giovanelli R., Gardner J. P., Connolly A. J., 2008, ApJ, 685, L13
Chang T.-C., Pen U.-L., Bandura K., Peterson J. B., 2010, Nature, 466, 463
Davé R., Katz N., Oppenheimer B. D., Kollmeier J. A., Weinberg D. H., 2013, MNRAS, 434, 2645
Davis M., Huchra J., 1982, ApJ, 254, 437
Delhaize J., Meyer M. J., Staveley-Smith L., Boyle B. J., 2013, MNRAS, 433, 1398
Driver S. P., Robotham A. S. G., 2010, MNRAS, 407, 2131
Efstathiou G., Ellis R. S., Peterson B. A., 1988, MNRAS, 232, 431
Fernández X. et al., 2013, ApJ, 770, L29
Freudling W. et al., 2011, ApJ, 727, 40
Giovanelli R. et al., 2005, AJ, 130, 2598
Haynes M. P. et al., 2011, AJ, 142, 170
Henning P. A. et al., 2010, AJ, 139, 2130
Hopkins A. M., Beacom J. F., 2006, ApJ, 651, 142
Keres D., Yun M. S., Young J. S., 2003, ApJ, 582, 659
Kim H.-S., Power C., Baugh C. M., Wyithe J. S. B., Lacey C. G., Lagos C. D. P., Frenk C. S., 2013, MNRAS, 428, 3366
Lagos C. D. P., Baugh C. M., Lacey C. G., Benson A. J., Kim H.-S., Power C., 2011, MNRAS, 418, 1649
Lagos C. d. P., Bayet E., Baugh C. M., Lacey C. G., Bell T. A., Fanidakis N., Geach J. E., 2012, MNRAS, 426, 2142
Lagos C. D. P., Baugh C. M., Zwaan M. A., Lacey C. G., Gonzalez-Perez V., Power C., Swinbank A. M., van Kampen E., 2014, MNRAS, 440, 920
Martin A. M., Papastergis E., Giovanelli R., Haynes M. P., Springob C. M., Stierwalt S., 2010, ApJ, 723, 1359
Martin A. M., Giovanelli R., Haynes M. P., Guzzo L., 2012, ApJ, 750, 38
Masui K. W. et al., 2013, ApJ, 763, L20
Meyer M. J. et al., 2004, MNRAS, 350, 1195
Noterdaeme P. et al., 2012, A&A, 547, L1
Obreschkow D., Rawlings S., 2009, ApJ, 696, L129
Padmanabhan H., Choudhury T. R., Refregier A., 2015, MNRAS, 447, 3745
Power C., Baugh C. M., Lacey C. G., 2010, MNRAS, 406, 43
Prochaska J. X., Wolfe A. M., 2009, ApJ, 696, 1543
Prochaska J. X., Herbert-Fort S., Wolfe A. M., 2005, ApJ, 635, 123
Quenouille M. H., 1949, Proc. Camb. Phil. Soc., 45, 483
Rao S. M., Turnshek D. A., Nestor D. B., 2006, ApJ, 636, 610
Rhee J., Zwaan M. A., Briggs F. H., Chengalur J. N., Lah P., Oosterloo T., van der Hulst T., 2013, MNRAS, 435, 2693
Rosenberg J. L., Schneider S. E., 2002, ApJ, 567, 247
Sault R. J., Teuben P. J., Wright M. C. H., 1995, in Shaw R. A., Payne H. E., Hayes J. J. E., eds, ASP Conf. Ser. Vol. 77, Astronomical Data Analysis Software and Systems IV. Astron. Soc. Pac., San Francisco, p. 433
Schmidt M., 1968, ApJ, 151, 393
Seljak U. et al., 2005, Phys. Rev. D, 71, 103515
Springob C. M., Haynes M. P., Giovanelli R., 2005, ApJ, 621, 215
Verheijen M., van Gorkom J. H., Szomoru A., Dwarakanath K. S., Poggianti B. M., Schiminovich D., 2007, ApJ, 668, L9
Westmeier T., Jurek R., Obreschkow D., Koribalski B. S., Staveley-Smith L., 2014, MNRAS, 438, 1176
Wolfe A. M., Gawiser E., Prochaska J. X., 2005, ARA&A, 43, 861
Wong O. I. et al., 2006, MNRAS, 371, 1855
Zwaan M. A., Briggs F. H., Sprayberry D., Sorar E., 1997, ApJ, 490, 173
Zwaan M. A., van Dokkum P. G., Verheijen M. A. W., 2001, Science, 293, 1800
Zwaan M. A. et al., 2003, AJ, 125, 2842
Zwaan M. A. et al., 2004, MNRAS, 350, 1210
Zwaan M. A., Meyer M. J., Staveley-Smith L., Webster R. L., 2005, MNRAS, 359, L30

SUPPORTING INFORMATION

Additional Supporting Information may be found in the online version of this paper:

Table A1. Parameters of the AUDS galaxies.
Figure A1. Spectra of the AUDS galaxies.
Figure A2. Spectra of the AUDS galaxies (cont.).
Figure A3. Spectra of the AUDS galaxies (cont.).
Figure A4. Spectra of the AUDS galaxies (cont.).
Figure A5. Spectra of the AUDS galaxies (cont.).
Figure A6. Spectra of the AUDS galaxies (cont.).
Figure A7. Spectra of the AUDS galaxies (cont.).
Figure A8. Spectra of the AUDS galaxies (cont.).
Figure A9. Spectra of the AUDS galaxies (cont.).
(http://mnras.oxfordjournals.org/lookup/suppl/doi:10.1093/mnras/stv1084/-/DC1).

Please note: Oxford University Press are not responsible for the content or functionality of any supporting materials supplied by the authors. Any queries (other than missing material) should be directed to the corresponding author for the paper.

This paper has been typeset from a TEX/LATEX file prepared by the author.